Study of the Relation Between the Reynolds Number and the Formation of Au and Ag Nanostructures by Flow-Driven Surface Modification in Microfluidic Reactors

Oscar Perez-Landeros *, Alan Garcia-Gallegos, David Mateos-Anzaldo, Roumen Nedev, Judith Paz-Delgadillo, Mariela Dominguez-Osuna, Evelyn Magaña-Leyva, Ricardo Salinas-Martinez, Mario Curiel-Alvarez

Posted Date: 25 March 2026

doi: 10.20944/preprints202603.1950.v1

Keywords: microfluidics; microreactors; nanostructures; plasmonic surfaces; galvanic displacement; flow-driven surface modification; additive manufacturing

 doi:10.20944/preprints202603.1950.v1

Article

Study of the Relation Between the Reynolds Number and the Formation of Au and Ag Nanostructures by Flow-Driven Surface Modification in Microfluidic Reactors

Oscar Perez-Landeros *, Alan Garcia-Gallegos, David Mateos-Anzaldo, Roumen Nedev, Judith Paz-Delgadillo, Mariela Dominguez-Osuna, Evelyn Magaña-Leyva, Ricardo Salinas-Martinez and Mario Curiel-Alvarez

Instituto de Ingeniería, Universidad Autónoma de Baja California, Blvd. Benito Juárez s/n, Mexicali 21280, Mexico

* Correspondence: oscar.manuel.perez.landeros@uabc.edu.mx

Abstract

Microfluidics enables spatially controlled nanostructure synthesis by coupling confined flows with surface reactions. In this work, we study how geometry-induced laminar micro-environments govern the in-situ formation of Au and Ag nanostructures inside 3D-printed microfluidic reactors. Proof-of-concept fish-scale valves were fabricated by masked stereolithography in three architectures designed to define three recurring zones in the microreactor, inside the scales (zone 1), between the scales (zone 2), and along the rows of scales (zone 3). A Cu thin film was deposited on the inner walls of the channel to serve as the sacrificial surface for galvanic replacement using $AgNO_3$ or HAuCl4. Distinct 0D, 1D, and 2D nanostructures were simultaneously obtained in a zone-dependent manner across the valves, including nanoparticle and nanopore-rich regions, nanowires, nanoflakes and clustered 2D features. COMSOL simulations were used to solve the Navier-Stokes equation and extract specific-zone flow descriptors, including Reynolds number, velocity, and wall shear stress, and relate them to the nanostructure morphologies observed by SEM. The flow throughout the devices is strongly laminar, with local Reynolds numbers up to 0.04, exhibiting systematic spatial gradients imposed by the valve geometry. These results provide a design-guided route to tune nanostructure morphology through microchannel architecture under constant global operating conditions.

Keywords: microfluidics; microreactors; nanostructures; plasmonic surfaces; galvanic displacement; flow-driven surface modification; additive manufacturing

1. Introduction

Over the last decade, microfluidics has seen its application in the synthesis of nanoparticles of noble metals [1–3], semiconductors [4], and metal colloids [5]. In particular, metallic and semiconductor nanostructures have been extensively studied due to their interaction with light, which can be used in various applications such as sensing, molecule capture, and degradation [6–8]. The fabrication of microfluidic chips includes an extensive study in the materials selection, and the substrate of choice as well; the most used materials in the fabrication of microchannels are polydimethylsiloxane (PDMS) [9], polymethyl methacrylate (PMMA), and polyvinyl chloride (PVC). Microfluidic devices expand the possibility of working with small sample volumes and enable portable devices for on-site testing [10]. Additionally, microfluidics has seen its way to even low-cost techniques by fabricating paper-based devices for the in situ synthesis of gold (Au) nanoparticles for the detection of biomarkers for a medical approach [11]. Likewise, a microfluidic chip has been

 doi:10.20944/preprints202603.1950.v1

reported that is capable of analyzing the biomechanical properties of blood for monitoring early-stage diseases [12]. Additive manufacturing (AM) is the process of producing a 3D object layer by layer, commonly using polymer filaments such as PLA (Polylactic Acid) or ABS (Acrylonitrile Butadiene Styrene) [13]. Vat photopolymerization (VP) is a subcategory of AM and has drawn attention due to its high printing resolution, easy production of complex geometries, and low energy and material consumption [14]. VP consists of a container that contains a photosensitive resin, which solidifies when exposed to ultraviolet light at a specific exposure time and intensity, obtaining a layer-by-layer 3D object with high resolution [15]. This method is an efficient way for rapid prototyping of rigid and flexible microfluidic devices in a variety of polymers.

These printed devices are not only useful as fluidic platforms but also enable the in situ synthesis of metallic nanoparticles within their internal microchannels. In this manuscript, a flow-driven, in-situ transformation of the Cu-coated microchannel surface by galvanic replacement was studied. Under constant global operating conditions, the fish-scale geometry creates distinct microenvironments (zones) that impose different dynamics of the local transport and reactions, yielding zone-dependent nanostructures along the reactor. In this context, the synthesis of metallic nanoparticles (NPs) was achieved through galvanic replacement reactions. The dominant variables in this method of synthesis, coupled with our microfluidic approach, are the characteristic length of the microchannel [16], the concentration of the solution [17], the flow rate [18], the pressure [19], and the reaction time [20]. In microchannel regimes, the flow parameters are characterized by laminar flow behavior with a Reynolds number (Re) less than 2000, making the modeling easier by using the Navier-Stokes equation compared to the chaotic behavior of turbulent regimes [21]. In this work, the Re number was studied, because it specifies the ratio between the effect of the inertial force vs the viscous force in the fluid flow. In microfluidic reactors, it is possible to obtain highly laminar flow, which, in terms of Re, corresponds to values ≤1. Therefore, the viscous force dominates the fluid. [22] Although vortices are not expected in a laminar regime, it is possible to achieve localized vortices. Reports have shown that tuning the geometry of microchannels can create microvortices, which serve as traps for particles and cells. [23] Noble metallic nanostructures are widely used in different areas, such as sensors for medical purposes [24,25], tribo nanogenerators for energy harvesting [26], and photocatalysis [27], among others. In this work, we estimate parameters that are not directly measurable, such as Re, shear stress, and flow velocity, using COMSOL simulations to relate them to the formation of metallic nanostructures by galvanic displacement in a laminar flow condition and to understand the role of the Re number in the synthesis of these nanostructures.

2. Materials and Methods

2.1. Chemical Reagents

The materials used for the fabrication of silver and gold nanostructures (NS) include high-purity Copper (Cu, Ted Pella 99.999%) for thermal evaporation, Silver Nitrate ($AgNO_3$, Sigma Aldrich, 99.0 %), and Tetrachloroauric Acid (HAuCl4, Sigma Aldrich, 99.9 %) for galvanic replacement. A microfluidic flow controller (Flow EZ, Fluigent) was used to drive and control reagent flow. The microfluidic reactors were made of transparent photosensitive resin.

2.2. Characterization Techniques

The fish valve areas, chemical composition, and morphology of the prepared NS were studied by scanning electron microscopy (SEM) and energy dispersive X-ray spectroscopy (EDS) using a Lyra FE-SEM from Tescan with a built-in Bruker EDS detector.

 doi:10.20944/preprints202603.1950.v1

2.3. Fabrication of the Microfluidic Chip

2.3.1. Design of the Microfluidic Fish Valve

Microfluidic chips were designed, fabricated, and studied in order to identify the key parameters of the flow-driven nanostructure synthesis. The microfluidic chips, also referred to as fish valves, were printed using the Masked Stereolithography (MSLA) technique, on an Anycubic Photon Mono 4K 3D printer, with a nominal resolution of 35 μm (X and Y axes) and 10 μm (Z axis), using Anycubic High Clear resin. The height of the microfluidic device was chosen to maintain a laminar regime and to locally alter the flow regime at specific zones within the microfluidic chip, aiming to achieve higher velocities and vortex spots. We fabricated three different versions of the microfluidic fish valve chips, each with a channel height of 200 μm. These valves contain an internal C-shaped scale-like microstructure that generates constant vortex spots and shifts the flow regime. The inner microstructures (referred to as scales) are uniformly distributed along the active surface of the devices, with 10, 33, and 100 scales for devices 1A, 2A, and 3A, respectively (Figure 1). The scales in devices 1A, 2A, and 3A are separated transversely to the flow direction (X axis) by 1.3 mm, 500 μm, and 150 μm, respectively, and along the flow direction (Y axis) by 1.3 mm, 600 μm, and 450 μm, respectively. The C-shaped scale-like structures have a height and width of 200 μm for all devices and a radius of 900 μm, 600 μm, and 250 μm for the 1A, 2A, and 3A devices, respectively. Table 1 summarizes the geometrical parameters of the three device types, and Figure 1 shows the spatial position of the dimensions. The total channel length and width in all three devices are 16 mm and 14 mm, respectively.

Table 1. Dimensions of characteristic features in the microfluidic fish valve devices 1A, 2A, and 3A.

Dimension / Label	1A	2A	3A
Scales quantity	10	33	100
Height (μm)	200	200	200
Width (μm)	200	200	200
Radius (μm)	900	600	250
x-distance (μm)	1300	500	150
y-distance (μm)	1300	600	450
Characteristic length l (μm)	91	84	77

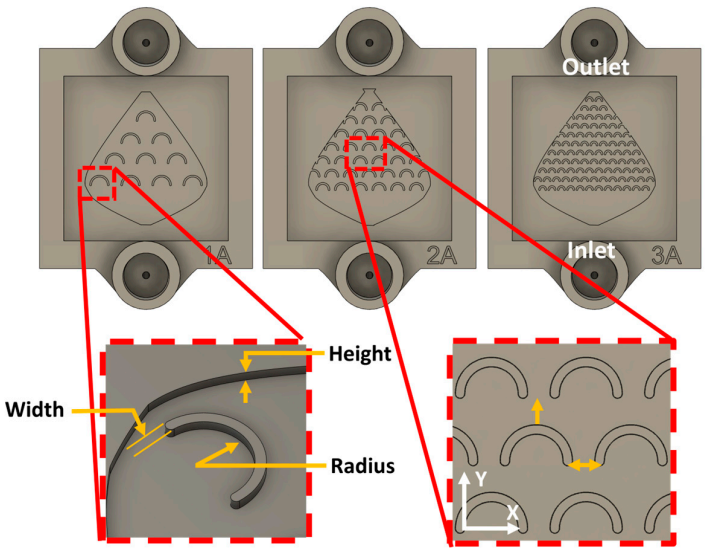

Figure 1. Definition of the zones of characteristic features in the 1A, 2A, and 3A fish valves.

 doi:10.20944/preprints202603.1950.v1

2.3.2. Thermal Evaporation Process

The bottom surface and walls of the channels were conformally coated with a 100 nm thick Cu film, deposited by a high-vacuum thermal evaporation technique at a pressure of 10^{-6} Torr. The chips were placed upside down in the chamber on a rotating holder at 45 RPM to ensure homogeneous coverage. A laser-cut Kapton mask defined the deposited area.

2.3.3. Window UV Cure

To complete the process, a transparent window was placed to seal the channels. A 2 cm × 2 cm, 500 μm-thick quartz square was attached to the top of the chip with a thin layer of photosensitive resin, cured by a focused UV laser. The window was intended to view the flow and reaction within the valve and for future optical analysis.

2.3.4. Galvanic Replacement Reaction

After completing the procedures described in Section 2.3.3, we proceeded to synthesize Ag nanostructures via galvanic replacement using a microfluidic pump (Fluigent Flow EZ), which can operate over a pressure range of 1–1000 mbar with 1 mbar resolution. Nitrogen was used as the operating gas in all experiments. A 1 mM solution of $AgNO_3$ was used as a precursor. The synthesis was conducted for 1 min at a constant flow rate of 10 μL/min. After this first experiment, the procedure was repeated using an $HAuCl_4$ solution (1 mM) to synthesize Au nanostructures using another set of microreactors. A total of six microfluidic devices were successfully processed and used for galvanic replacement experiments (three devices for Ag and three devices for Au). Devices that showed leakage or unstable flow/pressure response were excluded prior to synthesis. All experiments were performed at room temperature and atmospheric pressure.

2.3.5. Replicates and Spatial Sampling

To characterize the spatial variability of the formed nanostructures, using the same device, the microreactors were divided into zones, each zone containing the same microregions, as shown in Figure 2. The repeated microregions are: inside scales (zone 1), between the scales (zone 2), and along the rows of scales (zone 3). For each device, the number of available repeated regions was: 1A: zone 1 (n = 10), zone 2 (n = 14), zone 3 (n = 5); 2A: zone 1 (n = 33), zone 2 (n = 28), zone 3 (n = 8); 3A: zone 1 (n = 89), zone 2 (n = 97), zone 3 (n = 12).

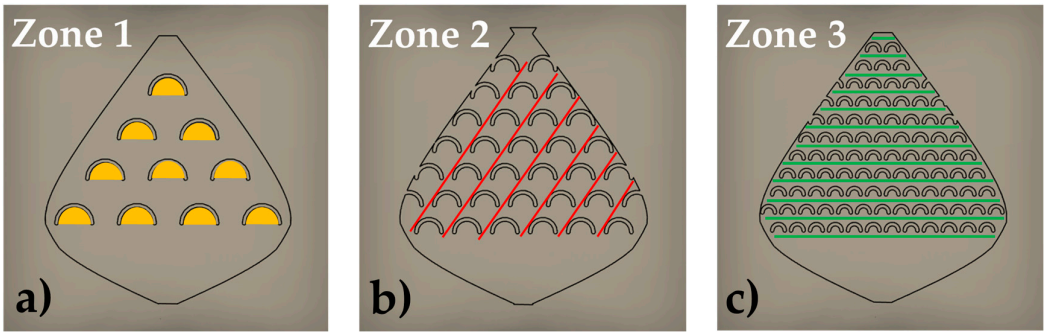

Figure 2. Schematic representation of the three zones of interest containing the three types of microregions: (a) inside the scales (zone 1), (b) between the scales (zone 2), and along the rows of scales (zone 3).

SEM inspection and measurements were performed following a row-based sampling scheme. For each device, at least one SEM image was analyzed per row for zone 1, at least one SEM image per row for zone 2, and at least one SEM image per representative location along the rows for zone 3. Because each device design contains a different number of rows, the total number of analyzed SEM

 doi:10.20944/preprints202603.1950.v1

images per zone varied across 1A–3A. Within each analyzed SEM image, characteristic nanostructure dimensions were measured and recorded to capture the dimensional range observed within each zone.

2.3.6. Simulation Model

The pressure, velocity, shear-stress distribution, and Re in the studied devices were estimated by COMSOL Multiphysics software. The fish valves used in the simulations were designed employing computer-aided design software, maintaining the same dimensions as the printed samples: a height of 200 μm, 16 mm long and 14 mm wide.

The Reynolds number was obtained by:

$$Re=\varrho ul/\mu \quad (1)$$

Where ϱ and μ are the density and dynamic viscosity of water, respectively (ϱ = 1000 kg/m^3 and μ = 0.001 Pa·s), l is the characteristic length (volume/area ratio) [28,29] of the channel shown in (Table 1), and u is the fluid velocity along the pathway obtained by simulation. The motion of the fluid through the device was obtained by solving the Navier-Stokes equation using COMSOL:

$$\varrho(u\cdot\nabla u)=\nabla\cdot[-pl+\mu(\nabla u+(\nabla u)\text{^}T\ )] \quad (2)$$

and the continuity equation:

$$\varrho\nabla\cdot(u)=0 \quad (3)$$

For this study, we assume an incompressible flow in the device and simplify the Navier-Stokes equation by neglecting gravity. For maximum accuracy in the simulation, we generated 104,085; 366,944; and 594,742 tetrahedral elements for 1A, 2A, and 3A devices, respectively. At the inlet, we define a fully developed flux velocity of 10 μl/min, equal to the one determined by the micropump Fluigent Flow EZ during the experiment. The boundary condition at the walls was set to u=0, with no slip. The outlet of the devices was set as a static pressure point (P=0).

3. Results and Discussion

3.1. Identification of Governing Flow Parameters

The fish-scale microchannel architecture defines three recurring micro-environments along the flow path in the three zones (Figure 2). The geometrical features impose zone-dependent hydrodynamic constraints at the Cu-coated surface: concave cavities promote low-velocity recirculation and localized vortices, whereas narrow gaps locally accelerate the flow and increase near-wall shear. Accordingly, the numerical model was used to extract velocity, shear stress, and Reynolds number fields to characterize the transport conditions within each zone.

To relate nanostructure formation to the governing flow parameters, we selected zones of interest where NS were predominantly observed throughout the device. The internal fish-scale microstructures promote localized vortices and recirculation whenever the flow interacts with the concave cavities, producing a heterogeneous distribution of velocities along the channel. Therefore, our analysis focuses on the regions where these geometry-induced perturbations may occur, primarily inside the scales, between adjacent scales, and along the edges of the valve. Numerical simulations show that the local Re remains very low throughout the device (Re ≤ 0.04 when using the scale spacing as the characteristic length). Inside the fish-scale cavities, Re decreases to the 10^{-3}–10^{-2} range, resulting in a creeping-like, viscosity-dominated flow with steady geometry-induced recirculation as shown in Figure 3a–c. In contrast, the regions between and along the scale rows exhibit slightly higher, yet still laminar, velocities (Re up to ≈ 0.04), consistent with accelerated flow through the narrow gaps between scales.

 doi:10.20944/preprints202603.1950.v1

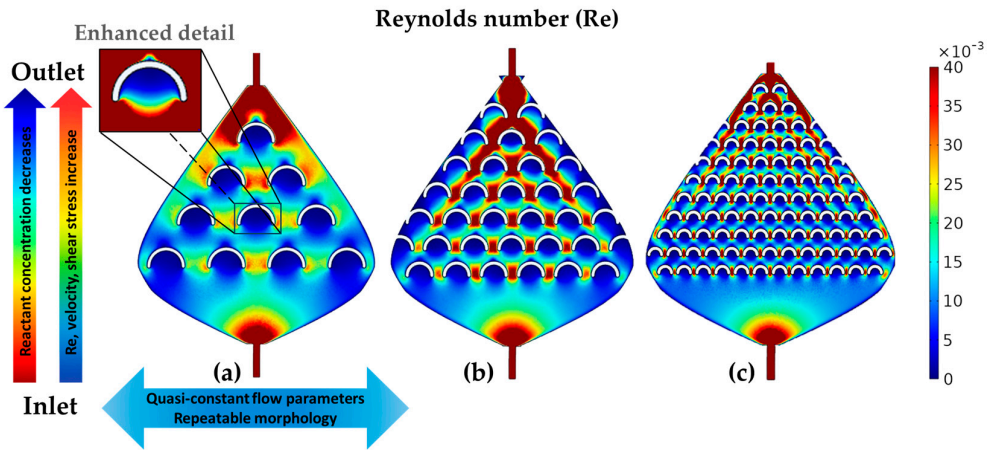

Figure 3. Reynolds number profiles for microreactor designs 1A, 2A, and 3A. The increasing Re, represented by a blue-to-red color scale, highlights well-defined zones of interest. The vertical arrows indicate variations in flow parameters and reactant concentration, while the horizontal arrow indicates quasi-static conditions across the microreactor width.

In addition to the Re, the flow velocity and shear stress profiles were extracted from the simulation results. The shear stress was calculated as the product of the shear rate and the dynamic viscosity, where the shear rate was provided by the simulation. The streamlines shown in Figure 4a represent the flow velocity magnitude, with the fastest flow depicted by red lines between the scales, and the slowest flow depicted by blue lines inside the scales, with intermediate flow velocities in the rest of the device areas. These three zones exhibit highly different velocity values, which match perfectly with the shear stress (Figure 4b) and Re results (Figure 3). Similarly, the nanostructures formed in these zones displayed a wide range of NS characteristics, as shown in Figures 5 and 6 in the section of experimental verification. The velocity magnitude, which depends on the flow rate, is important because of its relationship to the size and shape of the formed nanostructures [30], and because it can be directly controlled by the experimental setup. Similar simulation results were obtained for the flow in the three valves, with the most significant velocity increase between the scales in valve 3A, where the scales have the smallest lateral separation (x-axis). The flow velocity is qualitatively related to nanostructure formation as a function of reaction time, with the red lines corresponding to the minimum possible reaction time (Figure 4a) and the blue lines indicating a longer reaction time.

Because these maps were obtained under a single (fixed) set of boundary conditions, spatial changes in velocity and shear stress arise primarily from the channel geometry rather than from varying the driving conditions from run to run. Therefore, the three-zone partition provides a consistent framework for comparing the local hydrodynamic forcing with the SEM-observed morphologies (Figures 5 and 6) across 1A–3A.

Another variable considered is the wall shear stress. We plotted the shear stress along the channel surface (including walls and scales), and a representative map for valve 3A is shown in Figure 4b. Shear stress is particularly relevant under the present low-Reynolds-number conditions, where viscous effects dominate near-wall transport and surface reactions.

 doi:10.20944/preprints202603.1950.v1

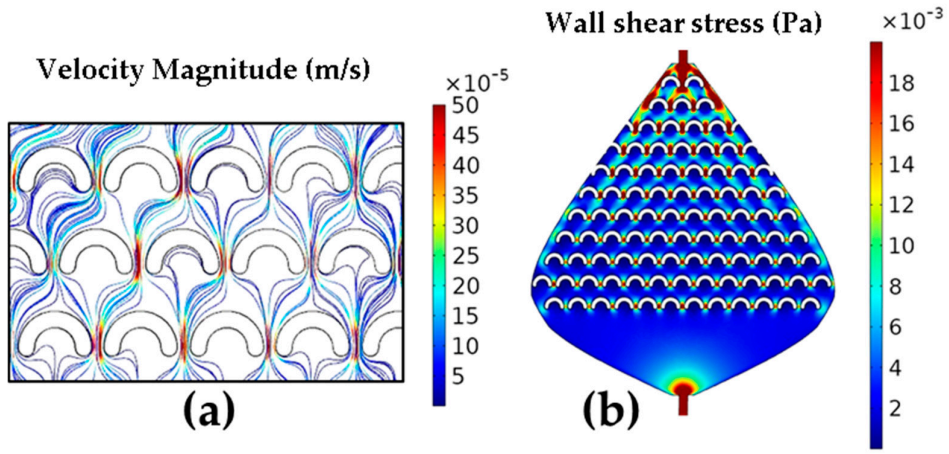

Figure 4. (a) Velocity magnitude and (b) Shear stress in the 3A microvalve shown in a blue-to-red scale.

The Re is related to the flow regime, which in turn influences how the precursor molecules interact with the surface of the nanostructures during galvanic displacement. Moreover, it is intrinsically related to other critical parameters, such as wall shear stress. As the Reynolds number increases, the wall shear stress also rises, as evidenced by the comparison of Figures 4(b) and 3(c) [31]. This relationship is crucial for NS formation, influencing the distribution of sizes and shapes of NS during the synthesis process. On the other hand, lower Re values inversely affect the residence time. Specifically, at low Re, the residence time increases, which explains the growth of larger NS (Figures 5c and 6c) due to a higher nucleation rate in regions of slow flow, as in the first rows of device 3A presented in Figure 2c.

A report on a microfluidic device used for the galvanic replacement of electrodeposited Cu in a solution of $AgNO_3$ on a p-type Si substrate [32], shows that at a low volumetric flow rate of 10 μL/min, the same as in the present study, Ag ions are deposited onto the substrate, resulting in the formation of spherical Ag nanoparticles. It also shows the correlation between wall shear stress and volumetric flow, which is a critical parameter in evaluating nanoparticle formation in a microfluidic device. Reports on the generation of metallic nanostructures in microfluidic devices [33], show that small increases in volumetric flow rate (4–8 μL/min) do not change the shape of the desired nanowall structures. However, a higher flow rate can lead to nanowalls with slightly larger dimensions due to a more efficient supply of reactants. In another report on the galvanic replacement of Cu nanostructures with a solution of $AgNO_3$ in a microfluidic device [34], it was determined that the optimal concentration of $AgNO_3$ at flow rate of 1 μL/min was 10 mM since at higher concentrations the mechanical strength of Ag-containing nanowalls is weak and the walls can be etched away. In the synthesis of Au-based nanostructures, there have been reports of reactions involving $HAuCl_4$, $H_3PW_{12}O_{40}$ (where PW is Phosphotungstic acid anion), and $H_3PMo_{12}O_{40}$ (where PMo is Phosphomolybdate anion) in a microfluidic device [35], resulting in the formation of decorated Au@POM (where POM is a mixture of PW and PMo, called Polyoxometalates) nanostructures within the microfluidic device at a volumetric flow rate of 1 mL/h for 2 h under constant UV irradiation.

At low velocities, mass transport toward the Cu surface becomes increasingly diffusion-limited, further enhancing nucleation in slow-flow regions. At low Reynolds numbers, where inertial effects are negligible, the viscous forces of the fluid dominate, controlling the transport of precursor molecules and their deposition onto the surface. The Re varies along the reactors (Figure 3), reaching its maximum values between the scales (zone 2) close to the outlet end of the valves. The minimum Re values were found near the first row of scales at the inlet side, where the fluid velocity is lowest. This behavior is expected by design and is observed across all scales and valves.

 doi:10.20944/preprints202603.1950.v1

3.2. Experimental Verification

The formation of nanoparticles in the microchannels of fish valves initiates with the interaction of $AgNO_3$ and $HAuCl_4$ with the Cu film coating the microchannels. The size and shape of the resulting Ag and Au nanoparticles depend on reactant concentration [36], flow velocity [37], residence time [38,39], shear stress [40,41], and Re [42]. Due to the passage of reagents through the intricate patterns of the microvalves, the concentration of $AgNO_3$ and $HAuCl_4$ is reduced towards the outlet. In addition, the flow velocity, shear stress, and Re vary significantly along the flow paths. These variations are critical for the kinetics of nanostructure formation. Any nanostructure can change its shape or disappear when the balance between reagent concentrations and flow parameters is disrupted [43].

The design of the three types of reactors (Figure 2), with microstructures (scales) arranged at strategic distances in order to modify fluid properties in a targeted manner, leads to the formation of various types of nanostructures (0D, 1D, and 2D) obtained in a laminar flow regime. The simulation results enabled the estimation of key parameters that cannot be directly measured, thereby allowing their correlation with nanostructures formed in specific zones. Three main zones within the microreactors were studied by SEM, those where the formed NS exhibited significant morphological differences: inside the scales, between the scales, and along the rows of scales (Figure 2).

3.2.1. Ag Nanostructures

The process occurring inside the microfluidic device is governed by a heterogeneous galvanic displacement reaction between Ag^+ ions in the 10 mM $AgNO_3$ solution and the Cu thin film coating the internal surfaces. In this reaction, Cu is oxidized to Cu^{2+}, releasing electrons that immediately reduce Ag^+ to metallic Ag on the Cu surface, forming nanostructures across the film. Because this interfacial mechanism is strongly influenced by local hydrodynamics, the number and spatial arrangement of the fish-scale features introduce regions with distinct flow characteristics, residence times, and shear conditions. Each of these regions functions effectively as a microscale flow valve, creating locally different synthesis conditions within the same device. Incorporating multiple scales, therefore, enables controlled modulation of nanostructure growth and allows systematic evaluation of how flow parameters govern nanostructure morphology and distribution.

In the three microreactors 1A, 2A, and 3A, semispherical nanoparticles (NPs) with diameters in the 300 - 500 nm range (Figure 5a) were observed in zone 1. Inside the scales, the smallest values of Re, shear stress, and flow velocity were obtained in all fish valve designs, allowing nucleation of particles in a steady-like flow. Additionally, some kinds of vortices were detected in this zone, hindering the replenishment of the scale cavities and limiting the reagent concentration and the galvanic replacement reaction. Figure 3a shows a detailed image of a scale with enhanced contrast, highlighting the Re distribution inside the cavity.

In the regions between the scales (zone 2), depicted as red lines (Figure 2b), nanowires (NWs) with widths ranging from ≤100 nm to 300 nm and lengths of 20–100 μm were formed (Figure 5b), primarily in device 3A, and less frequently in device 2A. As determined by the simulation, the Re, shear stress, and flow velocity between the scales reached their highest values, leading to the growth of elongated nanostructures as they were dragged in the flow direction. In device 2A, clusters of nanoflakes (NFs) were formed in the regions along the first 3-4 green lines (zone 3) near the microreactor inlet, where the $AgNO_3$ concentration was sufficient. The NFs were with a thickness of ~100 nm and a length between 1 and 3 μm (Figure 5c). The Re, shear stress, and flow velocity in zone 3 were intermediate compared to the previous two zones in all Ag and Au experiments.

 doi:10.20944/preprints202603.1950.v1

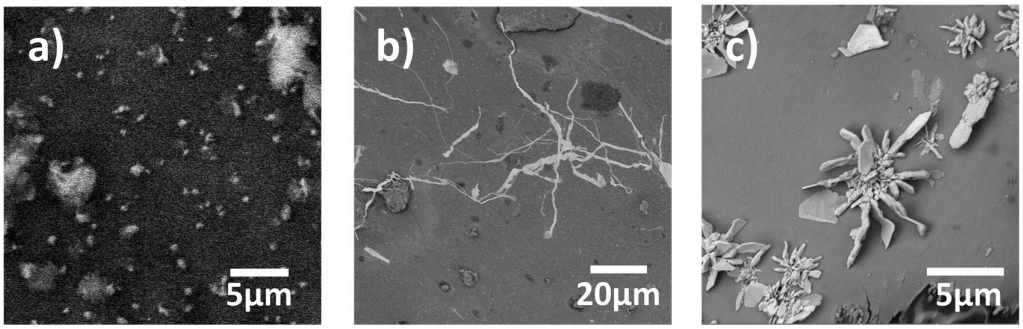

Figure 5. Ag nanostructures obtained within the microreactor channels: (a) Ag NPs with diameters ranging from 300 to 500 nm, formed in zone 1 of device 1A; (b) Ag NWs with widths between ≤100 and 300 nm, formed between the scales in zone 2 of device 3A; (c) clusters of Ag NFs with a thickness of ~100 nm, formed along the first 3–4 rows of scales in zone 3 near the microreactor inlet of device 2A.

3.2.2. Au Nanostructures

The flow parameters determined using COMSOL for the $HAuCl_4$ experiments were the same as for the Ag experiments in all zones and microreactor designs. In zone 1, in the region of the first 4-5 lines near the reactor inlet, NPs and nanopores were observed in the three microreactor designs (Figure 6a). The classical redox reaction leads to the formation of Au NPs with an average size of 50 nm and nanopores with a diameter $\leq$ 50 nm, driven by the reduction of Au and oxidation of Cu [44,45]. The nanopores are formed by corrosion due to the HCl byproduct, which decreases the pH of the solution [46]. In zone 2, Au NPs with diameters of 100 to 450 nm were observed in all microreactors (Figure 6b). The formation of larger diameter NPs is attributed to the replenishment of $HAuCl_4$ compared to zone 1. In zone 3, nanowalls with a thickness of ~100 nm and a length of about 5 µm were formed in the microreactor 3A (Figure 6c). The thickness was obtained when measured at the thinnest visible edges of the nanowalls. The transition from Au nanoparticles to nanowalls is consistent with zone-dependent local reaction conditions at the Cu-coated surface created by the valve architecture. Near the inlet, the precursor concentration is highest, and the local hydrodynamics include low-velocity recirculation and longer residence-time regions, which increase the local availability of Au species at the Cu-coated surface and promote coalescence and anisotropic growth into extended 2D wall-like features. Downstream and outside this localized region, the reactant concentration decreases along the reactor, and the local flow is more advective and shear-influenced in the narrow gaps, which favors repeated nucleation and the formation of discrete semi-spherical nanoparticles. This interpretation links the observed morphologies to the zone-resolved hydrodynamic fields obtained from the simulations. The nanowalls were observed only in the 3A microreactor at points where the minimum flow velocity values and the maximum residence time were obtained, due to flow resistance between scales. The maximum quantity of nanowalls was found along the first row of scales, where the $HAuCL_4$ concentration was enough to sustain the reaction. The quantity of nanowalls rapidly decreases and then becomes zero in the direction of the outlet, where the $HAuCl_4$ concentration decreases and the flow velocity increases.

 doi:10.20944/preprints202603.1950.v1

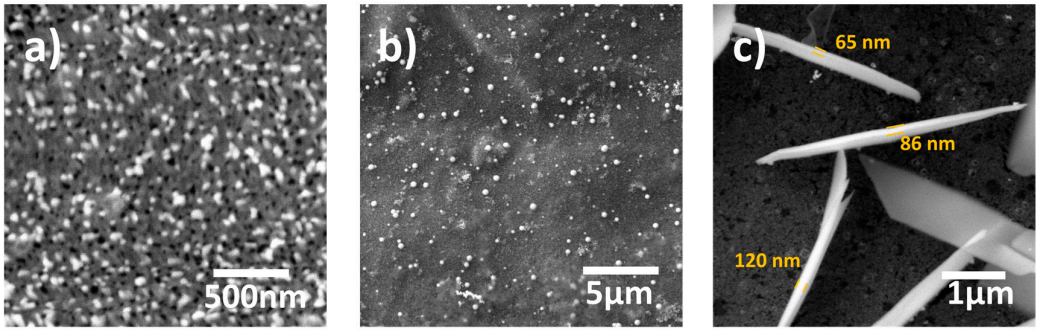

Figure 6. Au nanostructures obtained within the microvalve channels: (a) NPs and nanopores (black dots) with diameters ≤50 nm, formed in zone 1, in the first 4–5 lines close to the reactor inlet in device 1A; (b) Au NPs with diameters ranging from 100 to 450 nm, formed in zone 2 of device 3A; (c) Au nanowalls with a thickness of ~100 nm and a length of about 5 µm, formed near the inlet of device 3A.

3.2.3. Stability and Zone-Dependent Morphology

The stability of the proposed platform was assessed at the device and spatial levels. At the device level, operational robustness was ensured by pre-screening the valves for continuous flow and leak-free operation prior to synthesis, so that galvanic replacement was performed under stable nominal conditions. At the spatial level, stability refers to the repeatability of zone-dependent outcomes within a given architecture: across the inspected SEM regions, the dominant morphology recurred within each predefined zone across the device width, while variability was primarily reflected in characteristic size and areal density along the inlet-to-outlet direction, as summarized in Figure 3. A zone-resolved summary is provided in Table 2. These observations support the role of the fish-scale architecture in defining local micro-environments, such as concave cavities that promote low-velocity recirculation and localized vortices versus narrow gaps that locally accelerate the flow and increase the shear stress near the wall, which bias nucleation and growth pathways. Moreover, the architectural complexity provides repeated microregions within a single valve, enabling multiple internal comparisons within the same run and reducing run-to-run variability arising from handling and setup. Consequently, the valve design enables systematic spatial modulation of nanostructure morphology (0D/1D/2D) as a function of zone and geometry under the selected flow conditions, despite variability in characteristic size and areal density.

Table 2. Zone-resolved Re ranges and characteristic dimensions of Ag and Au nanostructures.

Device/Zone	Re range	Ag Nanostructures	Characteristic dimensions	Au Nanostructures	Characteristic dimensions
A1/Z1	8.28×10^{-04}–6.64×10^{-03}	NPs	300-500 nm	NPs, Nanopores	≤50 nm
A1/Z2	3.29×10^{-02}–5.58×10^{-02}	NPs	300-500 nm	NPs	100 - 450 nm
A1/Z3	8.02×10^{-03}–4.94×10^{-02}	NPs	300-500 nm	NPs	100 - 450 nm
A2/Z1	1.07×10^{-02}–3.60×10^{-02}	NPs	300-500 nm	NPs, Nanopores	≤50 nm
A2/Z2	1.08×10^{-01}–1.82×10^{-01}	NWs	≤100 - 300 nm	NPs	100 - 450 nm
A2/Z3	9.34×10^{-02}–1.10×10^{-01}	NFs	~100 nm	Nanowalls	~100 nm
A3/Z1	5.87×10^{-04}–1.33×10^{-02}	NPs	300-500 nm	NPs, Nanopores	≤50 nm

 doi:10.20944/preprints202603.1950.v1

A3/Z2	$5.46x10^{-02}$–$2.04x10^{-01}$	NWs	≤100 - 300 nm	NPs	100 - 500 nm
A3/Z3	$1.06x10^{-02}$–$1.43x10^{-01}$	NPs	300-500 nm	NPs	101 - 500 nm

In addition, these zone-dependent morphologies suggest practical routes for tailoring plasmonic surfaces within a single microfluidic platform. Nanoparticle and nanopore-rich regions can increase the density of curvature- and gap-driven electromagnetic hot spots, while wire-like and wall-like morphologies provide extended edges and junction networks that can further intensify localized fields. Therefore, the proposed architecture enables low-cost screening and spatial selection of plasmonic morphologies commonly associated with SERS substrates and biosensors, without requiring electrochemical processing.

5. Conclusions

This study successfully demonstrates the use of 3D-printed microfluidic devices for flow-driven surface modification and the synthesis of Ag and Au nanostructures via galvanic displacement, depending on microregion conditions. The unique internal geometries of the microreactors, characterized by C-shaped scale-like microstructures, allowed for the controlled formation of various nanostructures like nanoparticles, nanowires, nanoflakes, and nanowalls, through the modulation of flow parameters such as velocity, shear stress, and Reynolds number. Moreover, a strong relation was demonstrated between physical and chemical parameters (flow velocity and concentration gradient) and the nanostructure formation. Across the valve width, the dominant morphology in each zone was highly repeatable as confirmed by SEM, and variations were mainly observed along the flow direction from inlet to outlet. Lateral edge regions can deviate from the central pattern due to the intentionally asymmetric inlet-to-outlet design and local fabrication tolerances, which reduce symmetry. This spatial behavior is consistent with the zone-resolved hydrodynamic conditions summarized by the KPIs. The COMSOL simulations effectively correlated the flow characteristics with the observed nanostructure morphologies. The findings highlight the potential of these microfluidic systems to fine-tune the synthesis process toward applications such as surface enhanced Raman spectroscopy (SERS) and rapid prototyping of NPs based biosensors, without the need for electrochemical reactions. This approach supports low-cost, spatially resolved control of nanostructure morphology in microfluidic environments and provides a basis to design simplified valves that reproduce the determining local conditions to selectively obtain a target morphology.

Author Contributions: Conceptualization, O.P.-L.; methodology, O.P.-L. and E.M-L.; software, A.G.-G. and M.D.-O.; validation, M.D.-O. and J.P.-D.; formal analysis, R.N. and D.M.-A.; investigation, M.C-A. and R.N.; resources, O.P.-L., R.S.-M. and M.C-A.; data curation, A.G.-G. and E.M-L.; writing—original draft preparation, O.P.-L.; writing—review and editing, J.P.-D., R.S.-M. and D.M.-A.; visualization, O.P.-L; supervision, O.P.-L. All authors have read and agreed to the published version of the manuscript.

Funding: This research received no external funding.

Data Availability Statement: The data presented in this study are available on request from the corresponding author.

Acknowledgments: Alan Garcia-Gallegos and Evelyn Magaña-Leyva gratefully acknowledge the National Council for Science and Technology (CONACYT), Mexico, for providing Ph.D. and M.Sc. fellowships, respectively. We also thank Ivan Cardoza-Navarro for his assistance in experimental development, sample preparation, and formal analysis.

Conflicts of Interest: The authors declare no conflicts of interest.

 doi:10.20944/preprints202603.1950.v1

References

1. Sonexai, P., Van Nguyen, M., Huy, B. T., & Lee, Y.-I. (2023). Silver-based SERS substrates fabricated using a 3D printed microfluidic device. Beilstein Journal of Nanotechnology, 14, 793–803. https://doi.org/10.3762/bjnano.14.65
2. Lin, L., Li, X., Gao H., Xu, H., Starostin, S, A., Ostrikov, K. K., & Hessel, V. (2022). Microfluidic Plasma-Based Continuous and Tunable Synthesis of Ag-Au Nanoparticles and Their SERS Properties. Industrial & Engineering Chemistry Research , 61(5), 2183-2194. https://doi.org/10.1021/acs.iecr.1c04048
3. Bressan, L. P., Robles-Najar, J., Adamo, C. B., Quero, R. F., Costa, B. M. C., De Jesus, D. P., & Da Silva, J. A. F. (2019). 3D-printed microfluidic device for the synthesis of silver and gold nanoparticles. Microchemical Journal, 146, 1083–1089. https://doi.org/10.1016/j.microc.2019.02.043
4. Lu, X., Wang, H., & He, Y. (2022). Controllable Synthesis of Silicon-Based Nanohybrids for Reliable Surface-Enhanced Raman Scattering Sensing. Chinese Journal of Chemistry, 40(6), 734–745. https://doi.org/10.1002/cjoc.202100716
5. Hong, T., Lu, A., Liu, W., & Chen, C. (2019). Microdroplet Synthesis of Silver Nanoparticles with Controlled Sizes. Micromachines, 10(4), 274. https://doi.org/10.3390/mi10040274
6. Wu, J.Z.; Ghopry, S.A.; Liu, B.; Shultz, A. Metallic and Non-Metallic Plasmonic Nanostructures for LSPR Sensors. Micromachines 2023, 14, 1393. https://doi.org/10.3390/mi14071393
7. Antuña-Jiménez, D.; González-García, M.B.; Hernández-Santos, D.; Fanjul-Bolado, P. Screen-Printed Electrodes Modified with Metal Nanoparticles for Small Molecule Sensing. Biosensors 2020, 10, 9. https://doi.org/10.3390/bios10020009
8. Geng, H., Vilms Pedersen, S., Ma, Y., Haghighi, T., Dai, H., Howes, P. D., & Stevens, M. M. (2022). Noble metal nanoparticle biosensors: from fundamental studies toward point-of-care diagnostics. Accounts of chemical research, 55(5), 593-604. https://doi.org/10.1021
9. Yan, S., Chu, F., Zhang, H., Yuan, Y., Huang, Y., Liu, A., Wang, S., Li, W., Li, S., & Wen, W. (2019). Rapid, one-step preparation of SERS substrate in microfluidic channel for detection of molecules and heavy metal ions. Spectrochimica Acta Part A: Molecular and Biomolecular Spectroscopy, 220, 117113. https://doi.org/10.1016/j.saa.2019.05.018
10. Kuru, C. İ., Ulucan-Karnak, F., & Akgöl, S. (2023). 4—Lab-on-a-chip sensors: Recent trends and future applications. En A. Barhoum & Z. Altintas (Eds.), Fundamentals of Sensor Technology (pp. 65–98). Woodhead Publishing. https://doi.org/10.1016/B978-0-323-88431-0.00012-0
11. Pinheiro, T., Marques, A. C., Carvalho, P., Martins, R., & Fortunato, E. (2021). Paper Microfluidics and Tailored Gold Nanoparticles for Nonenzymatic, Colorimetric Multiplex Biomarker Detection. ACS Applied Materials & Interfaces, 13(3), 3576–3590. https://doi.org/10.1021/acsami.0c19089
12. Kang, Y. J. (2025). Microfluidic Chip for Quantitatively Assessing Hemorheological Parameters. Micromachines, 16(5), 567. https://doi.org/10.3390/mi16050567
13. Pagac, M., Hajnys, J., Ma, Q.-P., Jancar, L., Jansa, J., Stefek, P., & Mesicek, J. (2021). A Review of Vat Photopolymerization Technology: Materials, Applications, Challenges, and Future Trends of 3D Printing. Polymers, 13(4), 598. https://doi.org/10.3390/polym13040598
14. Chekkaramkodi, D., Jacob, L., C, M. S., Umer, R., & Butt, H. (2024). Review of vat photopolymerization 3D printing of photonic devices. Additive Manufacturing, 86, 104189. https://doi.org/10.1016/j.addma.2024.104189
15. Fiedor, P., Pilch, M., Szymaszek, P., Chachaj-Brekiesz, A., Galek, M., & Ortyl, J. (2020). Photochemical Study of a New Bimolecular Photoinitiating System for Vat Photopolymerization 3D Printing Techniques under Visible Light. Catalysts, 10(3), 284. https://doi.org/10.3390/catal10030284
16. Gosselin, D., Belgacem, M. N., Joyard-Pitiot, B., Baumlin, J. M., Navarro, F., Chaussy, D., & Berthier, J. (2017). Low-cost embossed-paper micro-channels for spontaneous capillary flow. Sensors and Actuators B: Chemical, 248, 395–401. https://doi.org/10.1016/j.snb.2017.03.144
17. Majee, S., & Shit, G. C. (2020). Modeling and simulation of blood flow with magnetic nanoparticles as carrier for targeted drug delivery in the stenosed artery. European Journal of Mechanics - B/Fluids, 83, 42–57. https://doi.org/10.1016/j.euromechflu.2020.04.004

 doi:10.20944/preprints202603.1950.v1

18. Lee, D., Kim, J., Park, Y., Lee, K.-H., Kim, C., Kwon, O., Kim, S., & Lee, S.-R. (2020). Sensitive and reliable thermal micro-flow sensor for a drug infusion system. Sensors and Actuators A: Physical, 309, 112033. https://doi.org/10.1016/j.sna.2020.112033
19. Cavazzuti, M., Corticelli, M. A., & Karayiannis, T. G. (2019). Compressible Fanno flows in micro-channels: An enhanced quasi-2D numerical model for laminar flows. Thermal Science and Engineering Progress, 10, 10–26. https://doi.org/10.1016/j.tsep.2019.01.003
20. Lu, H., Wang, H., Liu, Y., Wang, M., Hu, J., & Yang, Q. (2020). Substance transfer behavior controlled by droplet internal circulation. Chemical Engineering Journal, 393, 124657. https://doi.org/10.1016/j.cej.2020.124657
21. Mariotti, A., Antognoli, M., Galletti, C., Mauri, R., Salvetti, M. V., & Brunazzi, E. (2020). The role of flow features and chemical kinetics on the reaction yield in a T-shaped micro-reactor. Chemical Engineering Journal, 396, 125223. https://doi.org/10.1016/j.cej.2020.125223
22. Su, R., Wang, F., & McAlpine, M. C. (2023). 3D printed microfluidics: advances in strategies, integration, and applications. Lab on a Chip, 23(5), 1279-1299. https://doi.org/10.1039/d2lc01177h
23. Zhou, J., Kasper, S., & Papautsky, I. (2013). Enhanced size-dependent trapping of particles using microvortices. Microfluidics and nanofluidics, 15, 611-623. https://doi.org/10.1007/s10404-013-1176-y
24. Liu, X., Wang, J., Zhang, W., Ding, Z., Gu, J., Wang, Y., & Xu, Z. (2024). In-situ SERS monitoring of membrane receptor PTK7 for assessing cancer cell migration at single-cell level on a microfluidic chip. *Sensors and Actuators B: Chemical*, *404*, 135298. https://doi.org/10.1016/j.snb.2024.135298
25. Illath, K., Shinde, A., Paremmal, P., Gupta, P., Nagai, M., & Santra, T. S. (2023). Surface plasmon resonance tunable gold nanostar synthesis in a symmetric flow-focusing droplet device. *Surfaces and Interfaces*, *36*, 102478. https://doi.org/10.1016/j.surfin.2022.102478
26. Edith Navarro-Segura, M., Sánchez-Domínguez, M., Arizmendi-Morquecho, A., & Alvarez-Quintana, J. (2023). Triboelectric nanogenerator based on electrodeposited Ag octahedral nano-assemblies. *Journal of Energy Chemistry*, *83*, 478–495. https://doi.org/10.1016/j.jechem.2023.04.041
27. Li, G., Yang, C., He, Q., & Liu, J. (2022). Ag-based photocatalytic heterostructures: Construction and photocatalytic energy conversion application. *Journal of Environmental Chemical Engineering*, *10*(3), 107374. https://doi.org/10.1016/j.jece.2022.107374
28. Incropera, F. P., & Incropera, F. P. (Eds.). (2007). *Fundamentals of heat and mass transfer* (6th ed). John Wiley pp. 260.
29. Torres-Alvarez, D., Bosques-Palomo, B., Martínez-Dibildox, A., Marcos-Abdala, A., Jiménez-Nuñéz, R., Morones-Ramírez, J. R., Aeinehvand, M. M., & Aguirre-Soto, A. (2024). Introduction of the lowest printable (channel) characteristic length (LPCL) as a geometrical metric for the SLA 3D printing of embedded negative micro-structures. *Progress in Additive Manufacturing*. https://doi.org/10.1007/s40964-024-00788-6
30. Bressan, L. P., Robles-Najar, J., Adamo, C. B., Quero, R. F., Costa, B. M. C., De Jesus, D. P., & Da Silva, J. A. F. (2019). 3D-printed microfluidic device for the synthesis of silver and gold nanoparticles. *Microchemical Journal*, *146*, 1083–1089. https://doi.org/10.1016/j.microc.2019.02.043
31. Abo-Elkhair, R. E., Bhatti, M. M., & Mekheimer, Kh. S. (2021). Magnetic force effects on peristaltic transport of hybrid bio-nanofluid (Au Cu nanoparticles) with moderate Reynolds number: An expanding horizon. *International Communications in Heat and Mass Transfer*, *123*, 105228. https://doi.org/10.1016/j.icheatmasstransfer.2021.105228
32. Nie, Y., Jin, C., & Zhang, J. X. J. (2021). Microfluidic In Situ Patterning of Silver Nanoparticles for Surface-Enhanced Raman Spectroscopic Sensing of Biomolecules. ACS Sensors, 6(7), 2584–2592. https://doi.org/10.1021/acssensors.1c00117
33. Parisi, J., Liu, Y., Su, L., & Lei, Y. (2013). In situ synthesis of vertical 3-D copper-core/carbon-sheath nanowalls in microfluidic devices. RSC Adv., 3(5), 1388–1396. https://doi.org/10.1039/C2RA22183G
34. Parisi, J., Su, L., & Lei, Y. (2013). In situ synthesis of silver nanoparticle decorated vertical nanowalls in a microfluidic device for ultrasensitive in-channel SERS sensing. Lab on a Chip, 13(8), 1501. https://doi.org/10.1039/c3lc41249k
35. Lafuente, M., Pellejero, I., Clemente, A., Urbiztondo, M. A., Mallada, R., Reinoso, S., Pina, M. P., & Gandía, L. M. (2020). In Situ Synthesis of SERS-Active Au@POM Nanostructures in a Microfluidic Device for Real-

 doi:10.20944/preprints202603.1950.v1

Time Detection of Water Pollutants. ACS Applied Materials & Interfaces, 12(32), 36458–36467. https://doi.org/10.1021/acsami.0c06725

36. Xu, L., Peng, J., Srinivasakannan, C., Zhang, L., Zhang, D., Liu, C., Wang, S., & Shen, A. Q. (2014). Synthesis of copper nanoparticles by a T-shaped microfluidic device. RSC Adv., 4(48), 25155–25159. https://doi.org/10.1039/C4RA04247F
37. Yang, C.-H., Wang, L.-S., Chen, S.-Y., Huang, M.-C., Li, Y.-H., Lin, Y.-C., Chen, P.-F., Shaw, J.-F., & Huang, K.-S. (2016). Microfluidic assisted synthesis of silver nanoparticle–chitosan composite microparticles for antibacterial applications. *International Journal of Pharmaceutics*, *510*(2), 493–500. https://doi.org/10.1016/j.ijpharm.2016.01.010
38. Cai, Q., Castagnola, V., Boselli, L., Moura, A., Lopez, H., Zhang, W., De Araújo, J. M., & Dawson, K. A. (2022). A microfluidic approach for synthesis and kinetic profiling of branched gold nanostructures. Nanoscale Horizons, 7(3), 288–298. https://doi.org/10.1039/D1NH00540E
39. Yao, F., Wang, J., Zhang, W., Wang, Z., Li, Y., Sun, H., Chen, Q., & Liang, P. (2023). A microfluidic platform for minute-scale synthesizing Au@Ag nanocubes. *Materials Today Chemistry*, *34*, 101825. https://doi.org/10.1016/j.mtchem.2023.101825
40. Kang, T., Park, C., Meghani, N., Tran, T. T. D., Tran, P. H. L., & Lee, B.-J. (2020). Shear Stress-Dependent Targeting Efficiency Using Self-Assembled Gelatin–Oleic Nanoparticles in a Biomimetic Microfluidic System. *Pharmaceutics*, *12*(6), 555. https://doi.org/10.3390/pharmaceutics12060555
41. Kim, D., Lin, Y.-S., & Haynes, C. L. (2011). On-Chip Evaluation of Shear Stress Effect on Cytotoxicity of Mesoporous Silica Nanoparticles. *Analytical Chemistry*, *83*(22), 8377–8382. https://doi.org/10.1021/ac202115a
42. Khizar, S., Zine, N., Errachid, A., Jaffrezic-Renault, N., & Elaissari, A. (2022). Microfluidic-based nanoparticle synthesis and their potential applications. *Electrophoresis*, *43*(7-8), 819-838. https://doi.org/10.1002/elps.202100242
43. Parisi, J., Dong, Q., & Lei, Y. (2015). In situ microfluidic fabrication of SERS nanostructures for highly sensitive fingerprint microfluidic-SERS sensing. *RSC Advances*, *5*(19), 14081–14089. https://doi.org/10.1039/C4RA15174G
44. Ott, A., Bhargava, S. K., & O'Mullane, A. P. (2012). A study of the galvanic replacement reaction at surfaces and the role of lateral charge propagation. Surface Science, 606(1–2), L5–L9. https://doi.org/10.1016/j.susc.2011.09.012
45. Zhao, D., Xiong, X., Qu, C.-L., & Zhang, N. (2014). Remarkable Enhancement in Au Catalytic Utilization for Liquid Redox Reactions by Galvanic Deposition of Au on Cu Nanoparticles. The Journal of Physical Chemistry C, 118(33), 19007–19016. https://doi.org/10.1021/jp500908e
46. Zhong, X., Liu, P., Wen, J., Qiu, Y., Zhang, M., Xie, D., Wang, S., Xie, S., & Cheng, F. (2024). An in-situ method for SERS substrate preparation and optimization based on galvanic replacement reaction. Analytica Chimica Acta, 1303, 342512. https://doi.org/10.1016/j.aca.2024.342512